

Dual-domain point diffraction interferometer

Patrick P. Naulleau and Kenneth A. Goldberg

The phase-shifting point diffraction interferometer has recently been developed and implemented at Lawrence Berkeley National Laboratory to meet the significant metrology challenge of characterizing extreme ultraviolet projection lithography systems. Here we present a refined version of this interferometer that overcomes the original design's susceptibility to noise attributed to scattered light. The theory of the new hybrid spatial- and temporal-domain (dual-domain) point diffraction interferometer is described in detail and experimental results are presented. © 1999 Optical Society of America

OCIS codes: 050.1970, 050.5080, 120.2650, 120.3180, 260.7200.

1. Introduction

The emergence of extreme ultraviolet (EUV) projection lithography has placed stringent demands on interferometric metrology systems. To achieve diffraction-limited performance, EUV lithographic systems require wave-front tolerances of the order of 0.02 waves rms (0.3 nm rms at a wavelength of 13.4 nm).¹ Although the accuracy of interferometry is typically limited by the quality of the reference surface or wave, a high-accuracy class of interferometers has been developed in which the reference wave is created by diffraction from a small aperture.^{2,3}

One such interferometer is the phase-shifting diffraction interferometer developed by Sommargren.^{4,5} In this interferometer the reference wave is generated by diffraction from a single-mode optical fiber, providing the accuracy required for testing EUV lithographic systems. Use of optical fibers, however, restricts this interferometer to visible light with wavelengths approximately 40 times longer than those used in EUV lithography. This limit prevents the phase-shifting diffraction interferometer from measuring the phase effects of wavelength-specific reflective multilayer coatings used in EUV lithographic optics.

To accurately probe phase effects in these resonant reflective structures, at-wavelength EUV metrology is required. At-wavelength methods have the additional advantage of requiring less accuracy when de-

fining as a fraction of the measurement wavelength used. For example, an EUV interferometer with an accuracy of $\lambda_{\text{EUV}}/100$ is equivalent to a visible light interferometer with an accuracy of the order of $\lambda_{\text{VIS}}/4000$. This difference has significant impact on the ease of implementation. An important advantage of the visible light interferometer, however, is that it is a more feasible in-shop technique and provides the ability to measure individual uncoated optical elements.

Various at-wavelength interferometric measurement techniques, including lateral-shearing interferometry⁶ and Foucault and Ronchi testing,⁷ have been reported. These methods, however, have yet to demonstrate the accuracy required for the development of EUV lithographic imaging systems. To meet the accuracy challenge, an EUV-compatible diffraction-class interferometer, the phase-shifting point diffraction interferometer (PSPDI), was developed by Meddecki *et al.*⁸ The reference wave front in this interferometer has been demonstrated to have a systematic-error-limited accuracy⁹ of 0.05 nm, and the PSPDI has been used successfully in the testing of various prototype EUV lithographic systems.^{10,11} One of the drawbacks of the PSPDI, however, is its susceptibility to scatter in the optic under test that can cause confusion during analysis. In the presence of scattered light, the reference beam is no longer a clean spherical wave, but includes high-frequency features that make the interferometry more difficult. Midspatial frequency features in the wave front of interest are especially vulnerable to this problem.

In general, phase-shifting interferometers¹²⁻¹⁴ do not require use of a spatial carrier. This is due to the fact that the phase-encoding modulation occurs in the temporal domain; therefore a spatial carrier is

The authors are with the Center for X-Ray Optics, Lawrence Berkeley National Laboratory, Berkeley, California 94720.

Received 8 September 1998; revised manuscript received 1 March 1999.

0003-6935/99/163523-11\$15.00/0

© 1999 Optical Society of America

not required to unambiguously recover the phase information from the interferogram. From the point of view of accuracy and resolution, it is often desirable to operate without a spatial carrier. However, by design, the PSPDI forces a spatial carrier to be present. Nonetheless, the PSPDI is preferable to the conventional point diffraction interferometer configuration^{2,3} because of its ease of phase shifting and greatly increased optical throughput.⁸

The presence of the spatial carrier in the PSPDI makes it possible to perform the data analysis in the spatial domain using static-fringe analysis methods such as the Fourier-transform method.¹⁵ However, as previously implemented, the PSPDI is not optimized for this type of analysis. Typically, the time-domain analysis method has been used because it is impervious to spatial variations in the illumination or detector sensitivity.

Here we present an alternative configuration in physical implementation and data analysis, referred to as the dual-domain point diffraction interferometer, in which the PSPDI spatial carrier becomes an asset. The dual-domain analysis method is a hybrid of spatial and temporal processing that is capable of eliminating noise that neither the temporal-domain nor the spatial-domain analysis methods alone can suppress. It is essentially a three-tiered filtering system composed of a low-pass spatial filtering of the test-beam electric field, a bandpass spatial filtering of the individual interferogram irradiance frames of a phase-shifting series, and a bandpass temporal filtering of the phase-shifting series as a whole.

In Section 2 we begin with a review of the PSPDI as previously implemented and explain its susceptibility to scattered reference light. We then demonstrate how the Fourier-transform method,¹⁵ a spatial-frequency-domain static-fringe analysis method, can be used to suppress a significant portion of the scattered reference light noise. Finally, the dual-domain method is introduced using Fourier-domain analysis to prove the assertion that scattered reference light noise is fully separable with this technique.

2. Original Description of the Phase-Shifting Point Diffraction Interferometer

The PSPDI as shown in Fig. 1 is briefly described here; a more complete description can be found in the literature.^{8,10,11} The PSPDI is a variation of the conventional point diffraction interferometer^{2,3} in which a transmission grating has been added and the semi-transparent membrane typically used in conventional point diffraction interferometers has been replaced by a patterned opaque and transparent mask (the PSPDI mask in Fig. 1). These changes add phase-shifting capability and greatly improve the optical throughput of the system by alleviating the need to attenuate the test beam. In the PSPDI, the optical system under test is illuminated by a spherical wave generated by a pinhole placed in the object plane of the system under test. To guarantee the quality of the spherical wave illumination, the pinhole is chosen to be significantly smaller than the

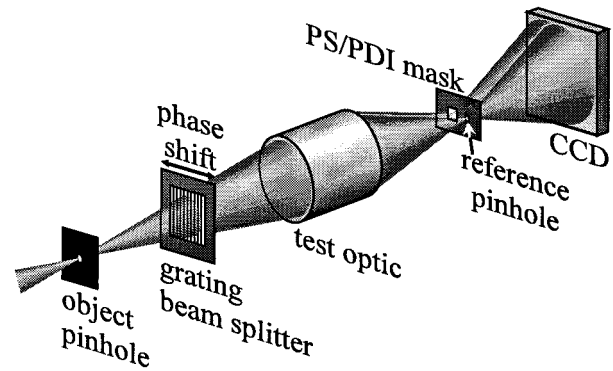


Fig. 1. Schematic of the PSPDI.

resolution limit of the optical system. The grating splits the illuminating beam to create the required test and reference beams. Lateral translation of this grating provides the relative phase shift between the test and the reference beams required for phase-shifting interferometry. The PSPDI mask, placed in the image plane of the optical system under test, blocks the unwanted diffracted orders generated by the grating and spatially filters the reference beam using a second pinhole (the reference pinhole). The test beam contains the aberrations imparted by the optical system and passes largely undisturbed through a window in the PSPDI mask that is large relative to the point-spread function (PSF) of the optical system under test. The spatial filtering of the reference beam provided by the reference pinhole removes the aberrations imparted by the optic. The test and reference beams propagate to the mixing plane where they overlap to create an interference pattern recorded on a CCD detector. The recorded interferogram yields information on the deviation of the test beam from the spherical reference beam.

The original description of the PSPDI⁸ requires the image-plane beam separation to be sufficient to prevent the reference beam from passing through the test-beam window. For a given separation, this requirement places limits on the magnitude of scattering and aberrations that can be present in the optic under test. If these limits are not met, the accuracy of the PSPDI is compromised.

3. Fourier-Transform Fringe Analysis Method (Spatial Frequency Domain)

PSPDI data analysis has been performed primarily using a time-domain phase-shifting method.^{8,10,11} Because of the PSPDI spatial carrier, however, it is also possible to perform the analysis using static-fringe methods such as the Fourier-transform method.¹⁵ In this section we consider the application of the Fourier-transform analysis method to PSPDI data. For the sake of brevity, we perform the following analysis in one dimension, considering only the dimension in the direction parallel to the image-plane beam separation; extension to the second lateral di-

mension is straightforward. Because the method presented here is primarily a filtering process, the analysis is most conveniently presented in the frequency domain.

We begin by considering the spatial spectrum of the electric field in the detector plane that is due to the reference-beam light alone. At the detector, the reference beam is a summation of the reference-beam light diffracted by the reference pinhole and the reference-beam light scattered through the window and can be written as

$$U_r(f_x) = A\delta(f_x - f_c) + \text{rect}\left(\frac{f_x}{W}\right)n(f_x), \quad (1)$$

where $n(f_x)$ is a complex-valued noise function representing the reference-beam light scattered through the window [$\text{rect}(\cdot)$], f_x is a variable representing spatial frequency, A is the reference-beam amplitude at the reference pinhole [the pinhole is approximated by $\delta(\cdot)$, the Dirac delta function], f_c is the separation between the pinhole and the center of the window in the spatial frequency domain, and W is the width of the window in the spatial frequency domain. The reference-beam light scattered through the window, the second term in Eq. (1), leads to the corruption we are trying to eliminate from the measurement. Because in the PSPDI there exists a Fourier-transform relationship between the signals in the image and detector planes, Eq. (1) is equivalent to the real-space reference-beam signal in the image plane, where $f_x \approx x/(\lambda z)$ with z being the distance between the image and detector planes.

Similarly, the spatial spectrum of the test beam in the detector plane can be expressed as

$$U_t(f_x) = \text{rect}\left(\frac{f_x}{W}\right)S(f_x), \quad (2)$$

where $S(f_x)$ is the test beam (PSF of the optic under test) including the scattered light in the test beam. The contribution of the test beam to the light making it through the reference pinhole was ignored because of its extremely small amplitude. Combining the test- and reference-beam terms in the detector plane yields

$$U(f_x) = A\delta(f_x - f_c) + \text{rect}\left(\frac{f_x}{W}\right)[n(f_x) + S(f_x)]. \quad (3)$$

This signal is graphically depicted in Fig. 2(a). For clarity, we ignored the details of the spatial spectrum shape of the light propagating through the window [$S(f_x)$].

This depiction of the field is based on the conventional PSPDI configuration, where f_c was chosen arbitrarily to be equal to the full width of the window. Here the criterion for choosing f_c , and the window width, is that the beam separation must be much greater than the width of the optical system PSF. This criterion comes from the desire that an insignificant amount of reference-beam light passes through

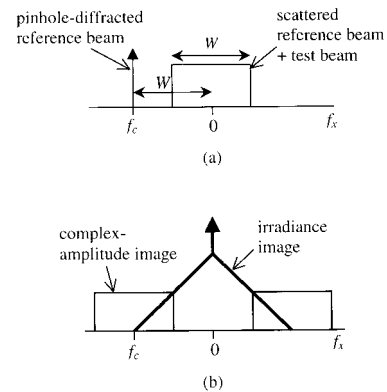


Fig. 2. Spatial spectrum of (a) the field in the recording plane and (b) the recorded irradiance for the standard PSPDI mask case.

the window. In the presence of scatter or high-frequency defects, the PSF is broad and the separation criterion becomes difficult to meet. Increasing the beam separation to strictly meet the requirement above can generate unacceptably high fringe density. Inadequate beam separation is what leads to the scatter susceptibility problem of the PSPDI. Also, appropriate beam separation may be difficult to achieve in the case in which large aberrations lead to a PSF that is much larger than the diffraction-limited PSF.

The interferogram that is actually recorded by the detector is irradiance, or equivalently, the modulus squared of the inverse Fourier transform of $U(f_x)$ [Eq. (3)]. By way of the autocorrelation theorem, we can see that the spatial spectrum of the recorded signal is the autocorrelation of $U(f_x)$ as depicted in Fig. 2(b). The central triangular peak is the zero-order term; this is essentially the irradiance of the light passing through the window. The two off-axis components are the positive and negative first-order terms that arise from the interference between the pinhole-diffracted reference beam and the light passing through the window. Either one of these first-order components can be used to recover the complex amplitude of the light passing through the window, assuming they are separable from the zero order.

In terms of Fourier-domain analysis, there is clearly a problem with the configuration in Fig. 2: The first-order components are not completely separated from the zero order in the spatial frequency domain. It is also important to note that, in this configuration, high-frequency noise terms from the zero-order map to low-frequency terms in the signal because the overlap reaches to the center of the signal passband. For this reason, we say that the current PSPDI configuration is not optimized for Fourier-domain analysis, which, strictly speaking, requires full separation of the orders. This point of view is well understood in the realm of electronic holography.¹⁶ As described above, the depictions in Fig. 2 are based on the simplifying assumption of the test beam having a flat spectrum. This assumption leads to significant energy in the wings of the zero

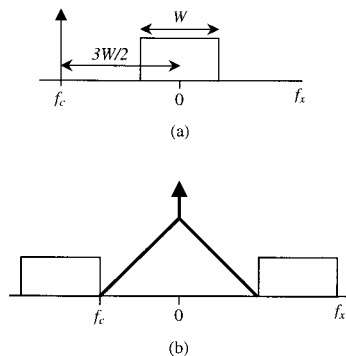


Fig. 3. Spatial spectrum of (a) the field in the recording plane and (b) the recorded irradiance for the spatial-analysis-optimized PSPDI mask case.

order. In practice the window is chosen to be many times larger than the width of the test beam, leading to zero-order wings that are much smaller than those depicted in Fig. 2 (refer to the example in Fig. 4). Nevertheless, when high accuracy is the goal, complete beam separation over the spatial-frequency band of interest should be guaranteed.

The required beam separation can be achieved by increasing the carrier frequency (or equivalently the beam separation) from W to $3W/2$. Doing so will increase the fringe density by a factor of 1.5; therefore more detector resolution will be required. In our experience, this has not been a limiting factor. Another consequence of the increased beam separation is an increase in the hyperbolic-fringe distortion present in spherical reference systems. This effect is linear with separation and can be predicted, measured, and removed.⁹ An alternative to increasing the beam separation is to appropriately reduce the window size to yield the same effect, which would reduce the bandwidth of the measurement by a factor of 1.5. In this case, we trade bandwidth for scattered light noise suppression. Again, we did not find this to be a limiting factor in typical applications. The spatial-analysis-optimized configuration, in which the beam separation was increased to $3W/2$, is depicted in Fig. 3.

The above analysis is valid in the lateral direction parallel to the image-plane beam separation. The restrictions on the window size do not apply to the direction orthogonal to the beam separation because there is no concern of overlapping orders in this direction.

Because the scattered reference light interfering with the test beam is confined to the zero-order term of the interferogram, we can isolate this noise term from the signal by ensuring that the zero order does not overlap with the first orders. This is accomplished by using a properly configured mask as described above. Using a Fourier-domain digital filter, the Fourier-transform analysis method can be used to selectively extract the signal free of zero-order corruption. Having done so, the noise term that is due to the scattered reference light interfering with the

test beam is eliminated. However, from the presence of $n(f_x)$ in Eq. (3) we can see that this is not the entirety of the scattered reference light noise.

4. Dual-Domain Analysis Method

In this section we further demonstrate the point that the Fourier-transform analysis method alone cannot eliminate the scattered reference light noise. Moreover, we prove the assertion made in Section 1 that the temporal-domain analysis method applied to phase-shifting data also suffers from scattered reference light noise. Finally, we describe a hybrid spatial and temporal processing technique (the dual-domain method) that is capable of completely eliminating the scattered reference light corruption problem.

We begin this discussion with the definition of several terms. The various interference components are defined according to their spatial frequency content while distinguishing the signal of interest from noise terms.

$$(1) \text{ Signal: } \text{rect}\left(\frac{f_x - f_c}{W}\right)S(f_x - f_c).$$

which is the pinhole-diffracted reference beam interfering with the test beam propagating through the window.

$$(2) \text{ Baseband noise: } \text{rect}\left(\frac{f_x}{W}\right)n(f_x) \otimes \text{rect}\left(\frac{f_x}{W}\right)S(f_x),$$

where \otimes represents the cross-correlation operator. This is the reference beam scattered through the window interfering with the test beam. The spatial spectrum of this noise term is limited to the autocorrelation width of the window and is centered at zero spatial frequency, hence it is referred to as baseband noise.

$$(3) \text{ Passband noise: } \text{rect}\left(\frac{f_x - f_c}{W}\right)n(f_x - f_c).$$

which is the reference beam scattered through the window interfering with the pinhole-diffracted reference beam. The spatial spectrum of this noise term occupies the same spatial frequency region as the signal, hence it is called passband noise.

To gain a better understanding of the scattered reference light corruption problem for the spatial- and temporal-domain analysis methods, we consider the recorded interferogram in more detail. The method presented here relies on the frequency-domain separability of the signal and noise terms. Therefore a natural description of the method involves expressing the recorded interferogram in the frequency domain as opposed to the more conventional spatial form $a(x) + b(x)\cos[2\pi f_c + c(x)]$. This approach is used routinely in the realm of Fourier optics and, more specifically, holography. From this point of view, the recorded interferogram is seen in terms of interferometric orders, where the modulated

light makes up the positive and negative first orders and the unmodulated light makes up the zero order.

We begin by considering the spatial-frequency-domain (Fourier-transform) analysis from Section 3 in more detail. The spectrum of the recorded interferogram consists of the autocorrelation of Eq. (3). This can be written in the form $\{\delta(f_x) + \Gamma[a(f_x)]\} + a(f_x - f_c) + a^*(f_x + f_c)$, where $\Gamma[a(x)]$ is defined as the autocorrelation of $a(x)$. These three terms are the zero order and the positive and negative first order, respectively, as depicted in Figs. 2(b) and 3(b). Performing this operation on Eq. (3), we find the zero order and positive first order to be

$$\text{first order} = \text{rect}\left(\frac{f_x - f_c}{W}\right)[n(f_x - f_c) + S(f_x - f_c)], \quad (4a)$$

$$\text{zero order} = \delta(f_x) + \Gamma\left\{\text{rect}\left(\frac{f_x}{W}\right)[n(f_x) + S(f_x)]\right\}. \quad (4b)$$

Relative amplitudes were ignored because they are irrelevant to the argument presented here. The Fourier-transform analysis consists simply of extracting the first order by using a bandpass filter in the spatial frequency domain and inverse Fourier transforming.¹⁵ In this case, even if we correct the spatial-order separation problem discussed above by setting f_c to $3W/2$ instead of W , there is a corruption problem caused by the appearance of both the signal and the passband noise in the first spatial order of the interferogram.

Next we show that temporal-domain analysis of phase-shifting interferometric data is also susceptible to the deleterious effects of beam overlap in the image plane. To perform temporal-domain analysis we require a series of interferograms with varying phase shifts between the test and the reference beams. Demodulation is performed on a pixel-by-pixel basis by examining the evolution of the intensity at each pixel throughout the temporal series. Because temporal-domain analysis of phase-shifting data is essentially a temporal filtering process and we are again interested in the frequency-domain separability of the signal and noise term, it is useful to express the signal in both temporal frequency and spatial frequency domains. To this end we rewrite Eq. (3) to include temporal frequency ν :

$$U(f_x, \nu) = A\delta(f_x - f_c, \nu - \nu_c) + \text{rect}\left(\frac{f_x}{W}\right) \times [n(f_x)\delta(\nu - \nu_c) + S(f_x)\delta(\nu)]. \quad (5)$$

Equation (5) is the spectrum of the electric field in the detector plane in both the spatial and the temporal domains, where, without loss of generality, we assume the phase shifting to occur on the reference beam alone. The temporal carrier frequency ν_c is set by the number of phase-shifting cycles contained in the phase-shifting series. For the PSPDI described

here, phase shifting is accomplished by lateral translation of the grating beam splitter as shown in Fig. 1.

To see the effect of the temporal filtering process, we express the recorded interferogram time series as interferometric orders in the temporal domain. The spectrum of the recorded interferograms consists of the autocorrelation of Eq. (5) and can be separated into interferometric temporal orders as

$$\begin{aligned} \text{first order} = & \left[\text{rect}\left(\frac{f_x - f_c}{W}\right)S(f_x - f_c) \right. \\ & \left. + \text{rect}\left(\frac{f_x}{W}\right)n(f_x) \otimes \text{rect}\left(\frac{f_x}{W}\right)S(f_x) \right] \\ & \times \delta(\nu - \nu_c), \end{aligned} \quad (6a)$$

$$\begin{aligned} \text{zero order} = & \left\{ \Gamma\left[\text{rect}\left(\frac{f_x}{W}\right)n(f_x) \right] \right. \\ & \left. + \Gamma\left[\text{rect}\left(\frac{f_x}{W}\right)S(f_x) \right] \right. \\ & \left. + \text{rect}\left(\frac{f_x - f_c}{W}\right)n(f_x - f_c) + \delta(f_x) \right\} \delta(\nu). \end{aligned} \quad (6b)$$

This is analogous to the representation in Eq. (4), where now the first order contains the time-varying (phase-shifting-modulated) intensity and the zero order contains the static (dc or unmodulated) component. The first temporal order is used to determine the phase at each pixel. Equation (6a) shows that both the signal and baseband noise contribute to the reconstructed wave front. The presence of the baseband noise in the first order is the PSPDI scatter problem mentioned above. The passband noise, however, appears only in the zero temporal order and thus does not contribute to the wave front reconstructed by the temporal-domain analysis method.

Although neither the Fourier-transform analysis (static-fringe) nor the temporal-domain analysis methods alone can fully eliminate the scattered reference light noise, it is important to note that as the reference pinhole gets smaller, making the reference beam weaker, the temporal-domain analysis method becomes more vulnerable to the scattered light noise, whereas the static-fringe analysis method does not. This is because the energy contained in both the signal and the passband noise diminish proportionally as the pinhole-diffracted reference light diminishes; thus the scattered-light-induced signal-to-noise ratio in the static-fringe analysis method, which suffers from passband noise corruption, is independent of pinhole size. On the other hand, the baseband noise energy is independent of the energy in the pinhole-diffracted reference beam; thus the scattered-light-induced signal-to-noise ratio in the temporal-domain analysis case drops as the pinhole-diffracted reference light diminishes (the pinhole gets smaller). This is problematic because the fundamental accuracy (reference-wave-limited accuracy) of the PSPDI

improves as the reference pinhole gets smaller,^{9,17} but at the same time, the temporal-domain analysis method becomes more vulnerable to scattered reference light noise. Turning to the spatial-domain method alone is not the optimal solution because it lacks many of the beneficial attributes of the phase-shifting method and, as shown above, it is not completely free of scattered reference light noise.

Here we show that it is possible to perform the analysis in such a way that the phase-shifting benefits are maintained while suppressing all scattered reference light noise. Examination of Eqs. (4) and (6) shows that combining the two analysis methods can eliminate scattered reference light noise entirely, assuming that complete spatial-order separation is guaranteed. This opportunity comes from the fact that the only term to appear in the first order of both domains [Eqs. (4a) and (6a)] is

$$\text{rect}\left(\frac{f_x - f_c}{W}\right)S(f_x - f_c),$$

the isolated signal term.

Recovering the signal free of both baseband noise and passband noise is now straightforward. Digitally applying a spatial-domain zero-order blocking filter to each recorded element of the temporal (phase-shifting) series will eliminate the baseband noise. This can alternatively be implemented as bandpass filters centered on the first orders of each recorded interferogram. When the spatial carrier is properly chosen, there is a natural zero (imposed by the physical window in the PSPDI mask) in the spatial spectrum at the ends of the zero order; therefore imposing a digital filter after recording of the interferogram is no more restrictive than the physical window itself and no spatial frequency content is sacrificed.

At this point, we have a series of filtered interferograms in which the baseband noise has been suppressed. This is simply a bandpass spatial filtering process, and no phase recovery yet has occurred. The cleaned interferograms can be represented as a set in the spatial and temporal frequency domain as

$$\begin{aligned} I(f_x, \nu) = & \text{rect}\left(\frac{f_x - f_c}{W}\right)[n(f_x - f_c)\delta(\nu) \\ & + S(f_x - f_c)\delta(\nu - \nu_c)] + \text{rect}\left(\frac{f_x + f_c}{W}\right) \\ & \times [n^*(f_x + f_c)\delta(\nu) + S^*(f_x + f_c)\delta(\nu - \nu_c)], \quad (7) \end{aligned}$$

which is the autocorrelation of Eq. (5) with the spatial zero-order component suppressed. Alternatively we can rewrite the recorded signal as a function of time at some arbitrary spatial location x_0 as

$$I(t) = N(x_0) + |s(x_0)|\cos[2\pi\nu_c t + \phi_s(x_0)], \quad (8)$$

where $N(x)$ is the inverse Fourier transform of $n(f_x)$, $s(x)$ is the inverse Fourier transform of $S(f_x)$, and $\phi_s(x)$ is the phase of $s(x)$.

Although in the cleaned interferograms the baseband noise term is suppressed, the spatially modulated noise term (passband noise) remains. Because the remaining passband noise is separable from the signal in the temporal frequency domain, as is evidenced by Eqs. (7) and (8), we can now recover the signal free of any scattered reference light noise by performing the usual temporal-domain analysis on the phase-shifting data. With the dual-domain analysis method, we benefit from the scattered reference noise suppression properties of both methods. In addition, we realize the benefits of the phase-shifting method.¹²⁻¹⁴

We note that, in terms of processing efficiency, it is preferable to perform the spatial-domain filtering in frequency space as described here rather than performing a convolution operation in real space. The processing efficiency of the dual-domain technique can be optimized further by performing the spatial-domain filtering as part of the temporal-domain analysis, allowing the number of required Fourier-transform calculations to be significantly decreased. Optimization depends on the specific temporal-domain algorithm used and exploits the linearity of the Fourier transform and this method.

It has been stated previously that the PSPDI is not well suited to testing systems with relatively large aberrations.⁸ This statement comes from the beam separation requirements described above. The presence of large aberrations that broaden the PSF and cause reference light to pass through the window is physically no different from the effect of scatter. In confronting these potential problems, the dual-domain implementation, with a properly configured mask, extends the usefulness of the PSPDI to larger aberrations. Although the dual-domain technique is still limited by the measurement bandwidth constraints imposed by the window size, spurious interference terms limiting the accuracy of the measurement are suppressed.

5. Flexibility of the Dual-Domain Analysis Method

Full elimination of the scattered reference light problem using the dual-domain analysis method requires the optimized PSPDI mask design described above. However, this method is also useful in less restrictive cases, such as the conventional PSPDI mask case in which the window width is equal to the beam separation. Here the zero-order blocking filter (spatial) must be reduced in size relative to the full width of the zero order because the zero order extends to the center of the spatial passband of interest. Alternatively we can think of putting a bandpass filter centered on the ± 1 orders (spatial) of the interferogram. The trade-off between baseband noise elimination and resolution in the reconstructed wave front becomes evident. Because the interferogram is a real signal, we could alternatively use twice the real part of the single-sideband-filtered image. This bandpass filtering approach is equally relevant to the optimized mask case described above.

What we lose in the nonoptimized mask case is

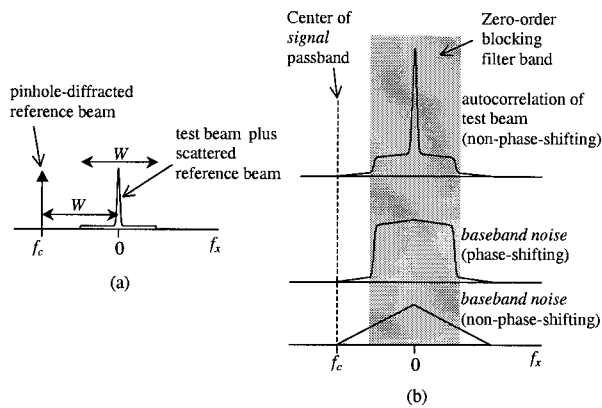


Fig. 4. (a) Spectrum of field at detector plane with standard PSPDI mask. The test beam is now comprised of a narrow central lobe and low-level scatter. (b) On-axis components of the detected irradiance spectrum. The y -axis scale is greatly exaggerated to show features. Also, the scaling is different for each component. The first component is the autocorrelation of the test beam. The second component is the cross correlation of the test beam and the scattered reference light. Finally, the third component is the autocorrelation of the scattered reference light. The dual-domain analysis method, applied to the standard PSPDI configuration, is capable of eliminating all scattered reference light noise except the phase-shifting baseband noise appearing in the signal passband.

some efficiency in baseband noise suppression. In practice, however, this loss of efficiency may be negligible. The spectral width of the baseband noise is determined by the cross correlation of the test-beam spectrum with the scattered reference light spectrum. The scattered reference light spectrum is limited by the width of the window and, in many practical situations, the test-beam spectrum is well approximated by a narrow peak (less than one tenth of the width of the test-beam window) along with low-level wings extending to the edges of the test-beam window. This situation leads to the concentration of baseband noise energy in an area that is not much larger than the test-beam window.

Figure 4 shows the standard mask configuration (as in Fig. 2) with a more realistic representation of the signal spectrum. In Fig. 4(a) we can see the spectrum of the field at the detector plane. The test beam is now comprised of a narrow central lobe and low-level scatter. Also contributing to the halo around the test-beam central lobe is the scattered reference light. Figure 4(b) depicts the on-axis components of the detected irradiance spectrum. The y -axis scaling is modified between components to make the features of interest visible. The first component is the autocorrelation of the test beam; this is the second element from the temporal zero order in Eq. (6). This component is non-phase-shifting; therefore the fact that it spills into the signal passband is irrelevant to the dual-domain analysis. The second component in Fig. 4(b) is the cross correlation of the test beam and the scattered reference light; this component is the second element from the temporal first order in Eq. (6) and is both phase shifting

and spills into the signal passband. Although the dual-domain analysis method cannot completely suppress this term in the standard mask configuration, we can see that a significant portion of it can indeed be eliminated. Finally, the third component in Fig. 4(b) is the autocorrelation of the scattered reference light; this is the first element from the temporal zero order in Eq. (6). This component is non-phase-shifting and poses no problem to the dual-domain analysis.

Figure 4 demonstrates that in practice the dual-domain method can be effective even without use of a dual-domain-optimized PSPDI mask. When applied to the less restrictive PSPDI mask configuration, this method is capable of eliminating all scattered reference light noise except the phase-shifting baseband noise appearing in the signal passband. In this configuration, the effectiveness of the dual-domain analysis method improves with the ratio of the test-beam central lobe to halo magnitude. In addition, the optimal zero-order blocking filter width is approximately the width of the window plus twice the width of the test-beam central lobe.

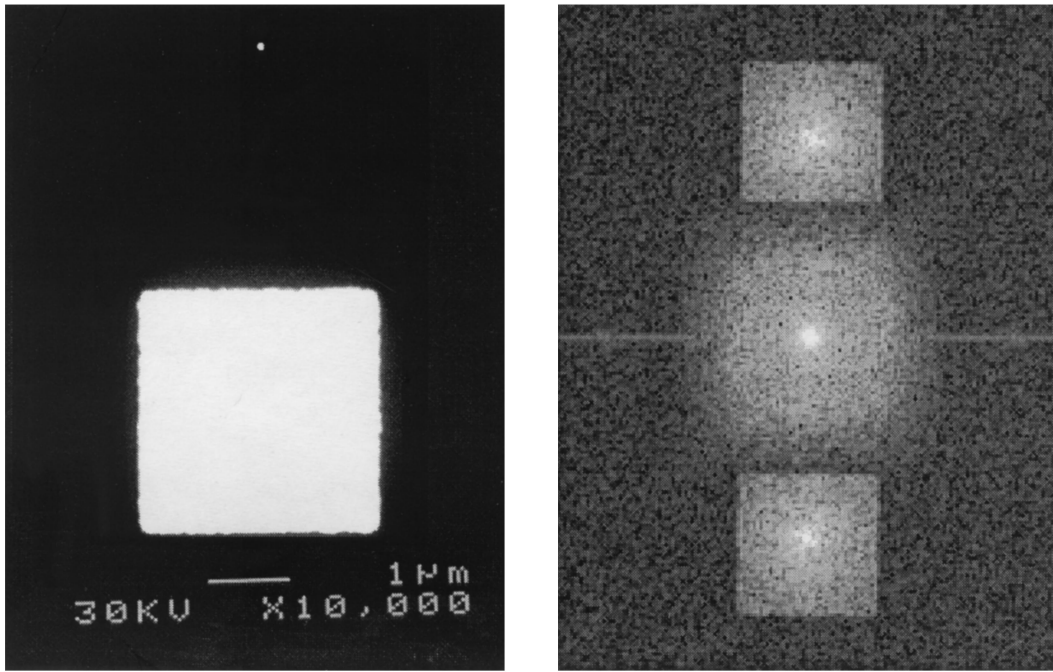
Considering a hypothetical case in which the ratio of the main lobe to halo magnitude is 10^6 , the FWHM of the PSF is 200 nm, and the beam separation and test-beam window width are $4.5 \mu\text{m}$, the nonoptimized dual-domain method can be shown to eliminate over 99% of the phase-shifting baseband noise. The fact that the zero-order blocking filter extends into the signal passband has the effect of reducing the effective test-beam window size (the size of the numerical spatial filter applied in the data processing). For this example, the effective test-beam window size is reduced by only 0.3 to $4.2 \mu\text{m}$.

6. Experimental Results

The methods presented here were verified with interferometric wave-front measurements on several prototype EUV $10\times$ demagnification Schwarzschild objectives designed for lithographic research.¹⁸ The Schwarzschild optic used for the specific results presented here has a rms wave-front error of $\sim 2 \text{ nm}$. The interferometry is performed using an undulator beamline¹⁹ at the Advanced Light Source Synchrotron Radiation Facility at Lawrence Berkeley National Laboratory. The beamline provides a tunable source of coherent EUV radiation.²⁰ The tests are performed at a wavelength near 13 nm, matching the designed operational wavelength of the test optics.

Figure 5(a) shows a scanning electron micrograph of the dual-domain analysis optimized mask with a window size of $3 \mu\text{m}$ and a pinhole-to-window center separation of $4.5 \mu\text{m}$. These masks are open stencil, fabricated using electron-beam lithography and reactive ion etching. In Fig. 5(b) we can see a log-scale image of the magnitude of the Fourier transform of the recorded intensity pattern when using the optimized mask. The desired spatial-frequency-domain separation between the first orders and the zero order is evident.

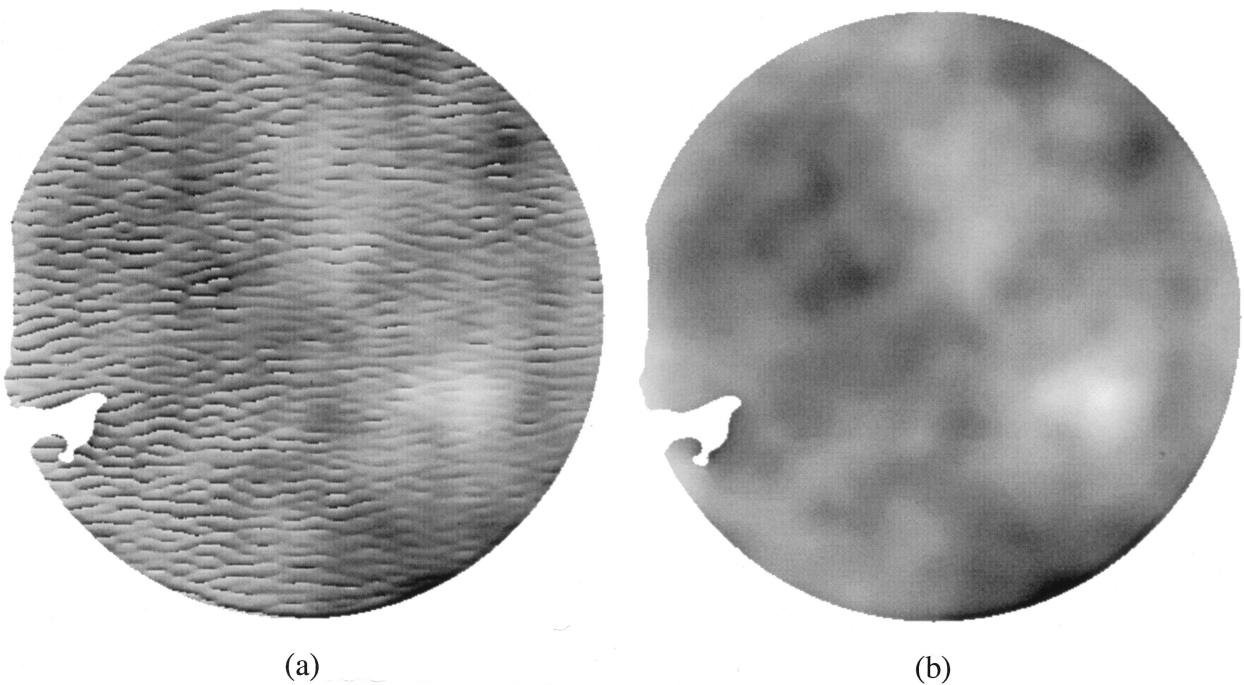
Figure 6 demonstrates the effectiveness of the



(a)

(b)

Fig. 5. (a) Scanning electron micrograph of the dual-domain analysis optimized mask with a window size of $3\ \mu\text{m}$ and pinhole-to-window center separation of $4.5\ \mu\text{m}$. (b) Log-scale image of the magnitude of the Fourier transform of the recorded intensity pattern when using the optimized mask.



(a)

(b)

Fig. 6. Wave front obtained (a) using the standard temporal processing (phase-shifting) technique and (b) using the dual-domain method. The same source data were used in both cases. The blanked-out regions of the wave front are areas where the test optic reflectance was too low to accurately measure the phase. The high-frequency features in (a) can be attributed to the baseband noise, which is not suppressed by conventional phase-shifting analysis.

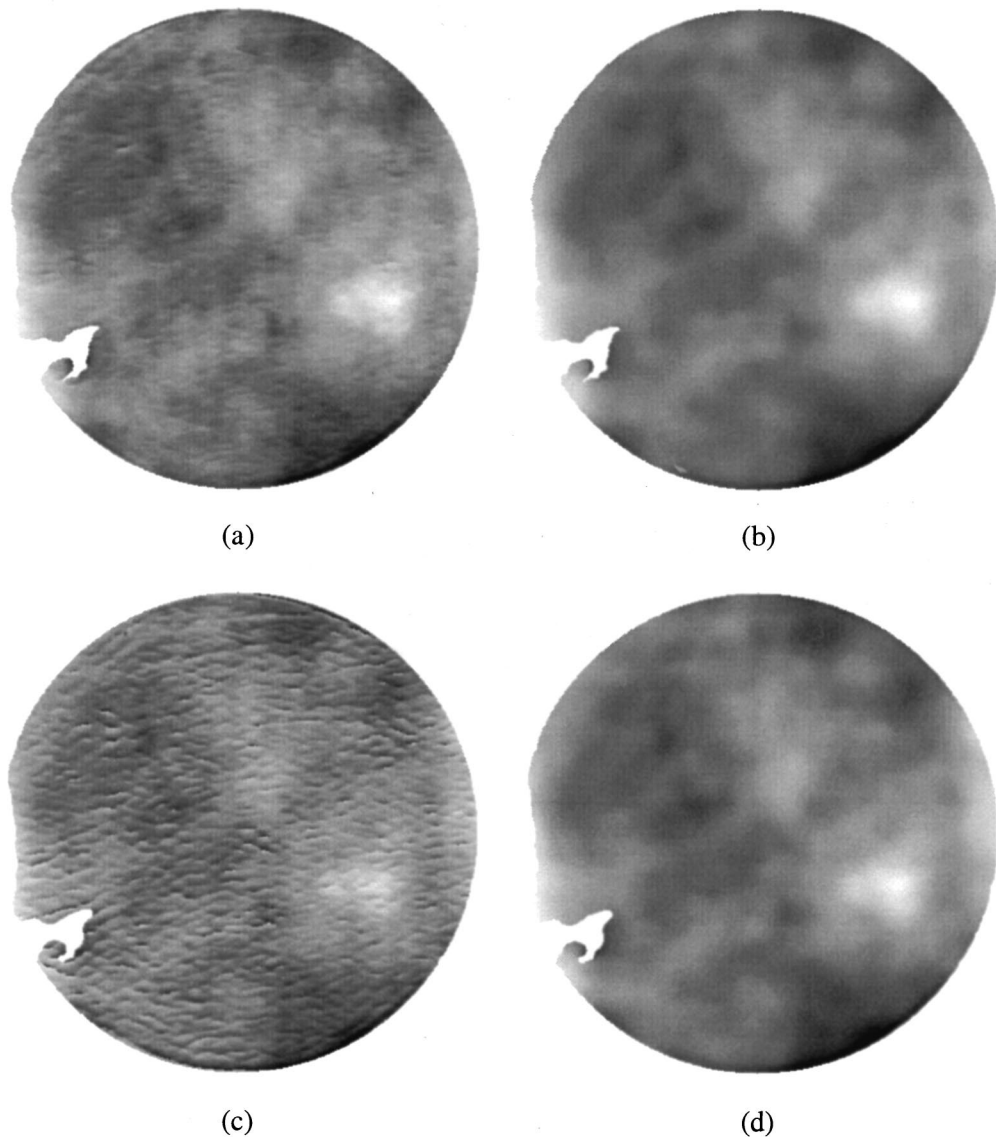


Fig. 7. Demonstration of the dual-domain analysis method applied to the standard PSPDI mask case. (a) Standard time-domain analysis and (b) dual-domain analysis with 200-nm reference pinhole. (c) Standard time-domain analysis with 100-nm reference pinhole, where scattered reference light noise is causing phase-retrieval errors. (d) Dual-domain analysis method with 100-nm reference pinhole.

dual-domain processing technique. The reference pinhole size in this case is 100 nm. Pinholes of this size have been shown previously⁹ to provide a reference wave accuracy of $\lambda_{\text{EUV}}/250$ (0.054 nm). For the test optic considered here, a reference pinhole that is this small is troublesome when using the standard PSPDI analysis because the reference light scattered through the window is of comparable magnitude to the pinhole-diffracted reference light. We note that the specific pinhole size at which this problem with the standard PSPDI becomes evident depends on the resolution and scatter characteristics of the particular optic being tested. Figure 6(a) shows the wave front obtained using standard temporal processing (phase-shifting) techniques. The blanked-out regions of the wave front are areas where the test optic reflectance was too low to accurately measure the

phase. The high-frequency features can be attributed to the baseband noise that is not suppressed by conventional temporal-domain analysis. These features are seen to cause serious phase retrieval errors. In Fig. 6(b) we can see the results for the same data set analyzed using the dual-domain method. The baseband noise has been effectively eliminated. The rms wave-front error for the dual-domain processing results is 2.13 nm, whereas the wave-front error is 2.72 nm using the conventional temporal-domain method. The rms of the difference wave front obtained from the wave fronts in Figs. 6(a) and 6(b) is 1.68 nm.

Figure 7 demonstrates the effectiveness of the dual-domain processing technique in the standard PSPDI mask configuration and shows that the technique becomes more important as the reference pin-

hole size decreases. Figure 7(a) shows the standard temporal processing results with a 200-nm reference pinhole. Again we can see the effect of baseband noise. The noise, however, is not strong enough to cause the phase retrieval to fail. Going to a smaller (100-nm) reference pinhole [Fig. 7(c)], we can see that the reduced signal-to-noise ratio causes serious phase-retrieval problems. Reprocessing the same sets of phase-shifting data using the dual-domain method adapted to the standard PSPDI mask configuration yields the results in Figs. 7(b) and 7(d) for the 200-nm and 100-nm reference pinhole cases, respectively. Comparing the dual-domain method with the conventional temporal-domain method, the rms of the difference wave fronts is 0.38 and 1.15 nm for the 200- and 100-nm reference pinhole cases, respectively.

We note that although the wave fronts in Figs. 6(a) and 7(c) show a considerable amount of noise, we can still perform low-order Zernike polynomial fitting with high accuracy. For example, the mean absolute-valued difference between the first 37 Zernike coefficients determined from Figs. 7(c) and 7(d) is only 0.08 nm. The primary benefits of the dual-domain analysis method are the extension of the useful spatial frequency range of the PSPDI measurement in the presence of scatter and the significant simplification of the required phase unwrapping procedures that are due to the removal of spurious high-frequency noise-induced features in the wave front.

7. Conclusions

We have demonstrated a new hybrid spatial- and temporal-domain point diffraction interferometer that is capable of suppressing the scattered reference light noise that hinders the conventional PSPDI. This method combines the separate noise-suppression capabilities of the widely used phase-shifting and Fourier-transform methods. A new optimized configuration for the PSPDI mask that eliminates the potential overlap of the test and reference beams in the spatial frequency domain of analysis has been presented. This mask enhances the performance of the new dual-domain analysis method and also improves the accuracy of the Fourier-transform method alone. Not limited to the optimized configuration, the dual-domain analysis method has also demonstrated performance enhancement with the nonoptimized standard PSPDI design.

The authors are greatly indebted to Erik Anderson for nanofabrication and to the entire staff at the Center for X-Ray Optics for supporting this research. We also acknowledge valuable discussions with Jeffrey Bokor. This research was supported by the EUV Limited Liability Company, the Defense Advanced Research Projects Agency, and the U.S. Department of Energy Office of Basic Energy Science.

References

1. D. M. Williamson, "The elusive diffraction limit," in *Extreme Ultraviolet Lithography*, D. Attwood and F. Zernike, eds., Vol. 23 of OSA Proceedings Series (Optical Society of America, Washington, D.C., 1995), pp. 68–76.
2. W. Linnik, "A simple interferometer to test optical systems," *Proc. Acad. Sci. USSR* **1**, 210–212 (1933).
3. R. N. Smartt and W. H. Steel, "Theory and application of point-diffraction interferometers," *Jpn. J. Appl. Phys.* **14**, Suppl. 14-1, 351–356 (1975).
4. G. E. Sommargren, "Phase shifting diffraction interferometry for measuring extreme ultraviolet optics," in *Extreme Ultraviolet Lithography*, G. D. Kubiak and D. R. Kania, eds., Vol. 4 of OSA Trends in Optics and Photonics (Optical Society of America, Washington, D.C., 1996), pp. 108–112.
5. G. E. Sommargren, "Diffraction methods raise interferometer accuracy," *Laser Focus World* **32**, 61–71 (1996).
6. J. E. Bjorkholm, A. A. MacDowell, O. R. Wood II, Z. Tan, B. LaFontaine, and D. M. Tennant, "Phase-measuring interferometry using extreme ultraviolet radiation," *J. Vac. Sci. Technol. B* **13**, 2919–2922 (1995).
7. A. K. Ray-Chaudhuri, W. Ng, F. Cerrina, Z. Tan, J. Bjorkholm, D. Tennant, and S. J. Spector, "Alignment of a multilayer-coated imaging system using extreme ultraviolet Foucault and Ronchi interferometric testing," *J. Vac. Sci. Technol. B* **13**, 3089–3093 (1995).
8. H. Medeck, E. Tejnil, K. A. Goldberg, and J. Bokor, "Phase-shifting point diffraction interferometer," *Opt. Lett.* **21**, 1526–1528 (1996).
9. P. Naulleau, K. A. Goldberg, S. Lee, C. Chang, C. Bresloff, P. Batson, D. Attwood, and J. Bokor, "Characterization of the accuracy of EUV phase-shifting point diffraction interferometry," in *Emerging Lithographic Technologies II*, Y. Vladimirov, ed., Proc. SPIE **3331**, 114–123 (1998).
10. E. Tejnil, K. A. Goldberg, S. H. Lee, H. Medeck, P. J. Batson, P. E. Denham, A. A. MacDowell, J. Bokor, and D. Attwood, "At-wavelength interferometry for EUV lithography," *J. Vac. Sci. Technol. B* **15**, 2455–2461 (1997).
11. K. A. Goldberg, E. Tejnil, S. H. Lee, H. Medeck, D. T. Attwood, K. H. Jackson, and J. Bokor, "Characterization of an EUV Schwarzschild objective using phase-shifting point diffraction interferometry," in *Emerging Lithographic Technologies*, D. E. Seeger, ed., Proc. SPIE **3048**, 264–270 (1997).
12. P. Carre, "Installation et utilisation du comparateur photoelectrique et interferential du bureau international des poids et mesures," *Metrologia* **2**, 13–17 (1966).
13. R. Crane, "Interference phase measurement," *Appl. Opt.* **8**, 538–542 (1969).
14. J. H. Bruning, D. R. Herriot, J. E. Gallagher, D. P. Rosenfeld, A. D. White, and D. J. Brangaccio, "Digital wavefront measuring interferometer for testing optical surfaces and lenses," *Appl. Opt.* **13**, 2693–2703 (1974).
15. M. Takeda, H. Ina, and S. Kobayashi, "Fourier-transform method of fringe-pattern analysis for computer-based topography and interferometry," *J. Opt. Soc. Am.* **72**, 156–160 (1982).
16. E. Leith, H. Chen, Y. Chen, D. Dilworth, J. Lopez, R. Masri, J. Rudd, and J. Valdmanis, "Electronic holography and speckle methods for imaging through tissue using femtosecond gated pulses," *Appl. Opt.* **30**, 4204–4210 (1991).
17. K. A. Goldberg, E. Tejnil, and J. Bokor, "A 3-D numerical study of pinhole diffraction to predict the accuracy of EUV point diffraction interferometry," in *Extreme Ultraviolet Lithography*, G. D. Kubiak and D. R. Kania, eds., Vol. 4 of OSA Trends in Optics and Photonics (Optical Society of America, Washington, D.C., 1996), pp. 133–137.
18. D. A. Tichenor, G. D. Kubiak, M. E. Malinowski, R. H. Stulen, S. J. Haney, K. W. Berger, R. P. Nissen, R. L. Schmitt, G. A.

- Wilkerson, L. A. Brown, P. A. Spence, P. S. Jin, W. C. Sweat, W. W. Chow, J. E. Bjorkholm, R. R. Freeman, M. D. Himel, A. A. MacDowell, D. M. Tennant, O. R. Wood II, W. K. Waskiewicz, D. L. White, D. L. Windt, and T. E. Jewell, "Development and characterization of a 10 \times Schwarzschild system for SXPL," in *Soft X-Ray Projection Lithography*, A. M. Hawryluk and R. H. Stulen, eds., Vol. 18 of OSA Proceeding Series (Optical Society of America, Washington, D.C., 1993), pp. 79–82.
19. R. Beguiristain, J. Underwood, M. Koike, P. Batson, E. Gulikson, K. Jackson, H. Medeck, and D. Attwood, "High flux undulator beam line optics for EUV interferometry and photoemission microscopy," in *High Heat Flux Engineering III*, A. M. Khounsary, ed., Proc. SPIE **2855**, 159–169 (1996).
20. D. Attwood, G. Sommargren, R. Beguiristain, K. Nguyen, J. Bokor, N. Ceglio, K. Jackson, M. Koike, and J. Underwood, "Undulator radiation for at-wavelength interferometry of optics for extreme-ultraviolet lithography," *Appl. Opt.* **32**, 7022–7031 (1993).